Available online at www.sciencedirect.com

ScienceDirect

Advances in Space Research 61 (2018) 673–682

ADVANCES IN SPACE RESEARCH (a COSPAR publication)

www.elsevier.com/locate/asr

Detailed analysis of dynamic evolution of three Active Regions at the photospheric level before flare and CME occurrence

Yudong Ye [a,b], M.B. Korsós [c,d,*], R. Erdélyi [c,e]

[a] SIGMA Weather Group, State Key Laboratory of Space Weather, National Space Science Center, Chinese Academy of Sciences, Beijing 100190, China
[b] University of Chinese Academy of Sciences, Beijing 100049, China
[c] Solar Physics & Space Plasma Research Center (SP2RC), University of Sheffield, Hounsfield Road, S3 7RH, UK
[d] Debrecen Heliophysical Observatory (DHO), Konkoly Astronomical Institute, Research Centre for Astronomy and Earth Sciences, Hungarian Academy of Sciences, P.O. Box 30, Debrecen H-4010, Hungary
[e] Department of Astronomy, Eötvös Loránd University, P.O. Box 32, Budapest H-1518, Hungary

Received 13 May 2017; received in revised form 15 September 2017; accepted 27 September 2017
Available online 7 October 2017

Abstract

We present a combined analysis of the applications of the weighted horizontal magnetic gradient (denoted as WG_M in Korsós et al. (2015)) method and the magnetic helicity tool (Berger and Field, 1984) employed for three active regions (ARs), namely NOAA AR 11261, AR 11283 and AR 11429. We analysed the time series of photospheric data from the Solar Dynamics Observatory taken between August 2011 and March 2012. During this period the three ARs produced a series of flares (eight M- and six X-class) and coronal mass ejections (CMEs). AR 11261 had four M-class flares and one of them was accompanied by a fast CME. AR 11283 had similar activities with two M- and two X-class flares, but only with a slow CME. Finally, AR 11429 was the most powerful of the three ARs as it hosted five compact and large solar flare and CME eruptions. For applying the WG_M method we employed the Debrecen sunspot data catalogue, and, for estimating the magnetic helicity at photospheric level we used the Space-weather HMI Active Region Patches (SHARP's) vector magnetograms from SDO/HMI (Solar Dynamics Observatory/Helioseismic and Magnetic Imager). We followed the evolution of the components of the WG_M and the magnetic helicity before the flare and CME occurrences. We found a unique and mutually shared behaviour, called the U-shaped pattern, of the weighted distance component of WG_M and of the shearing component of the helicity flux before the flare and CME eruptions. This common pattern is associated with the decreasing-receding phases yet reported only known to be a necessary feature prior to solar flare eruption(s) but found now at the same time in the evolution of the shearing helicity flux. This result leads to the conclusions that (i) the shearing motion of photospheric magnetic field may be a key driver for solar eruption in addition to the flux emerging process, and that (ii) the found decreasing-approaching pattern in the evolution of shearing helicity flux may be another precursor indicator for improving the forecasting of solar eruptions.

Keywords: AR; Flare; CME; Precursor parameters

1. Introduction

The magnetic field topology of a solar active region (AR) plays an important role in flare and coronal mass ejection (CME) processes. Shearing motion and flux emerging are viewed widely to be accountable for such eruptive changes in the magnetic field topology of an AR. Further, large CMEs are often associated with more energetic flares (Yashiro et al., 2006; Hudson, 2010), which is indicative of a potential common underlying physical mechanism of flares and CMEs.

* Corresponding author at: Solar Physics & Space Plasma Research Center (SP2RC), University of Sheffield, Hounsfield Road, S3 7RH, UK.
E-mail address: korsos.marianna@csfk.mta.hu (M.B. Korsós).

https://doi.org/10.1016/j.asr.2017.09.038
0273-1177/

Adjacent opposite magnetic polarities associated with the sites of large-scale eruptive events have their own strongly-sheared localised polarity inversion line (PIL) where the magnetic field gradient is high, which indicates the existence of intense electric currents and large free magnetic energy in the solar atmosphere (Schrijver, 2007). The free (non-potential) energy often becomes the energy source of flares and CMEs. Therefore regions around PILs are preferred areas of interest to search for reliable precursors of these dynamic events. A recent comparative review about the various forecasting methods and their capabilities for predicting solar eruptions can be found in, see e.g., Benz (2017) and Leka et al. (2017) and references therein.

Magnetic field is strongly sheared in flaring locations (Hagyard et al., 1990). Large-scale shearing is built up through the slow motion of footpoints which stretching the length of the loops and twisting them (Roudier et al., 2008). In the literature, the important condition of flux emergence is more widely accepted than the shearing motion of the footpoints of an AR to trigger solar flares (Chandra et al., 2009; Takafumi and Takaaki, 2014; Louis et al., 2015). A general concept is that new emerging magnetic flux (tube) may interact with the pre-existing flux (tubes) where magnetic reconnection may occur in the current sheet, which forms between the old and the new fluxes. In this process, the importance of the emergence of the flux may seem to outweigh the associated shearing of the magnetic field, leading to that focused by many on studying the various measures of flux emergence. By analysing magnetic helicity flux, especially its shearing component, we argue that shearing may also provide an important clue prior to flare and CME eruption.

Magnetic helicity in a volume V is defined by $H = \int_V \mathbf{A} \cdot \mathbf{B} dv$, where $\mathbf{B}$ is the magnetic field, and $\mathbf{A}$ is the corresponding vector potential which satisfies $\mathbf{B} = \nabla \times \mathbf{A}$. Magnetic helicity in an open volume condition, like in ARs, was first introduced by Berger and Field (1984) as a description of how the magnetic field is sheared or twisted when compared to a reference potential field (Berger, 1984). Analysing magnetic helicity provides insight into understanding the underlying mechanism of solar magnetic activities such as flare onsets and CMEs.

As a measure of non-potentiality of the solar magnetic field, magnetic helicity can either be generated by photospheric shearing motion or be transported across the photosphere through emerging of twisted magnetic structures (Zhang et al., 2012). During the evolution of magnetic field, the total magnetic helicity conservation cannot relax to a potential field. Therefore, the accumulated magnetic helicity could be a source of CME occurrence in a non-equilibrium state (Démoulin, 2007; Démoulin and Pariat, 2009). The amount of helicity stored in pre-flare structures determines whether a big flare will be eruptive or be confined (Nindos and Andrews, 2014).

In this article, we investigate three different ARs with the methods of the weighted horizontal magnetic gradient (denoted as WG_M) developed in Korsós et al. (2015) and magnetic helicity analysis (Berger, 1984; Berger and Field, 1984) for improving our flare/CME prediction capability. The complementary application of the two methods focuses on the evolution of an active region, including analysis of sunspot movements and changes in magnetic properties, to improve the potentials to predict flares and CMEs using pre-eruption parameters. All the three investigated active regions produced a series of flares and CMEs (see for the details Tables 1–3).

In Section 2, we describe the detailed analysis of three ARs by applying the WG_M method and by evaluating the evolution of their magnetic helicity, respectively. Then, Section 3 concludes about the dedicated complementary use of the WG_M method and the magnetic helicity calculation in terms of flare and CME forecasting capabilities.

Table 1
The examined properties of the AR 11261.

Flare	Flare onset time	v_{lin} of CME [km/s]	Maximum $WG_M \cdot 10^6$ [Wb/m]	Onset $WG_M \cdot 10^6$ [Wb/m]	T_C [h]	T_{D+F} [h]	T_{pred} [h]	S_{flare}	Decrease [%]
M9.3	30/07/2011 02:02	–	2.7	1.2	11	12	21.43	M9.9	55%
M1.4	02/08/2011 06:24	712	2.5	2.0	11	6	21.43	M9.1	22%
M6.0	03/08/2011 13:54	610	2.5	1.9	9	13	19.73	M9.1	27%
M9.3	04/08/2011 04:09	1315	1.5	1	29	17	36.73	M5.4	36%

Table 2
The examined properties of the AR 11283.

Flare	Flare onset time	CME $v_{lin.}$ [km/s]	Maximum $WG_M \cdot 10^6$ [Wb/m]	Onset $WG_M \cdot 10^6$ [Wb/m]	T_C [h]	T_{D+F} [h]	T_{pred} [h]	S_{flare}	Decrease [%]
M5.3	06/09/2011 01:35	782	0.7	1.0	13	30	17.88	M3.0	–
X2.1	06/09/2011 22:12	575	1.1	0.8	17	14	26.53	M3.8	24%
X1.8	07/09/2011 23:10	792	1.4	1.0	17	39	26.53	M5.2	26%
M2.7	09/09/2011 07:10	318	1.4	0.8	17	70	26.53	M5.2	43%

Table 3
The examined properties of the AR 11429.

Flare	Flare onset time	CME $v_{lin.}$ [km/s]	Maximum $WG_M \cdot 10^6$ [Wb/m]	Onset $WG_M \cdot 10^6$ [Wb/m]	T_C [h]	T_{D+F} [h]	T_{pred} [h]	S_{flare}	Decrease [%]
X1.1	05/03/2012 04:30	1531	3.5	2.5	10	11	20.58	X1.2	27%
X5.4	07/03/2012 00:02	2684	3.7	1.9	12	7	22.28	X1.3	48%
X1.6	07/03/2012 01:14	1825	3.7	1.8	12	8	23.98	X1.3	52%
M6.3	09/03/2012 03:22	950	3.7	0.5	11	13	21.43	X1.3	86%
M8.4	10/03/2012 17:15	1296	3.7	0.01	5	4	16.33	X1.3	98%

2. Analysis

2.1. Application of weighted horizontal magnetic gradient to three different ARs

First, we investigate the pre-flare and CME dynamics of AR 11261, AR 11283 and AR 11429 with the weighted horizontal magnetic gradient (denoted as WG_M) between two opposite magnetic polarity sunspot groups introduced by Korsós et al. (2015). The WG_M is a new proxy parameter that may characterise the evolution of the magnetic field in the flare and CME-producing domain of an AR. The WG_M is computed between two groups of nearby spots having opposite polarities, the flux amounts are summarised for the two groups and divided by the distance value:

$$WG_M = \left| \frac{\sum_i B_{p,i} \cdot A_{p,i} - \sum_j B_{n,j} \cdot A_{n,j}}{d_{pn}} \right|. \quad (1)$$

Here, B is mean the line of sight magnetic field and A denotes the corrected sunspot umbra area. The indices p and n denote positive and negative polarities, i and j are their running indices in the selected spot cluster. The distance (d_{pn}) is the separation between the center of gravity (or barycentre) of all the spots with the same polarity grouped together and that of the opposite polarity spots in the selected region. The selected region is fixed and the evolution (e.g. emergence of new spot or flux cancellation) of spot groups within this region is monitored (see for the detailed description of the investigated area in Korsós et al., 2015).

Here, for the analysis of the three ARs, AR 11261, AR 11283 and AR 11429, we employed the SDO/HMI-Debrecen sunspot data catalogue. This catalogue provides accurate and detailed Carrington-coordinates, mean estimated magnetic field from the line of sight magnetogram and projection-corrected area information for all observable sunspots and sunspot groups at an hourly basis from 2010 to the end of 2014 (see for the details in Baranyi et al., 2016).

The WG_M method is based on tracking changes of the solar surface magnetic configuration in ARs as flare precursors with about hourly time resolution, with the purpose of predicting energetic flares above M5. In Korsós et al. (2015), two diagnostic tools were introduced to probe the pre-flare behaviour patterns. The first one is based on the relationship between the values of the maxima of the WG_M and the intensity of the flare(s). The viability of the relationship in terms of flare forecast capability was tested on the largest available statistical sample of 61 cases observed during the era yielded by SOHO/MDI-Debrecen Data sunspot catalogue (Baranyi et al., 2016). It was concluded that this connection may provide useful insights into the relationship between the accumulated free energy, represented by WG_M as a proxy measure, and the released energy represented by the highest GOES-class in a set of homologous flares as another proxy measure. The second tool developed, the prediction of the flare onset time, is based on the relationship found between the duration of diverging motion of the barycenters of opposite polarities until the flare onset and duration of the compressing motion of the area-weighted barycenters of opposite polarities. These new proxies greatly enhance the capability of forecast, including *(i)* the expected highest intensity flare-class; *(ii)* the accuracy of onset time prediction and *(iii)* whether a flare, stronger than M5 in terms of the GOES classification scheme, is followed by another same energetic flare event(s).

In the last columns of Figs. 1–3, AR 11261, AR 11283 and AR 11429, respectively, are shown in their white-light appearance (upper panel) and the corresponding magnetogram (bottom panel). The red circles highlight the study area for the use of the WG_M method. The remaining panels of Figs. 1–3, i.e., the results derived from the analysis of the WG_M, shows the variation of the WG_M (top panel), distance (middle panel), and net flux (bottom panel) over the analysed time series are plotted. In Figs. 1–3, the vertical blue/green lines mark the M/X-class flares. The column (b) of Fig. 1 is associated with "Region 1" and column (c) with "Region 2".

We may state, in general, that the pre-flare behaviour of the weighted horizontal magnetic gradient applied to the three studied ARs confirms well, and, is in agreement with the results presented by Korsós et al. (2015). Indeed, we can recognise the distinguishing pre-flare behaviour of WG_M, i.e., that it has a steep rise and a high maximum value followed by a less steep decrease before the flare(s) occurred (upper panels of Figs. 1–3). Furthermore, by inspecting the middle panels of Figs. 1–3, we observed that the distance parameter shows the unique converging-diverging motion, often referred to as the U-shaped phase, prior to flare(s) which is a necessary condition for the reconnection processes associated with flares (see Korsós et al., 2015).

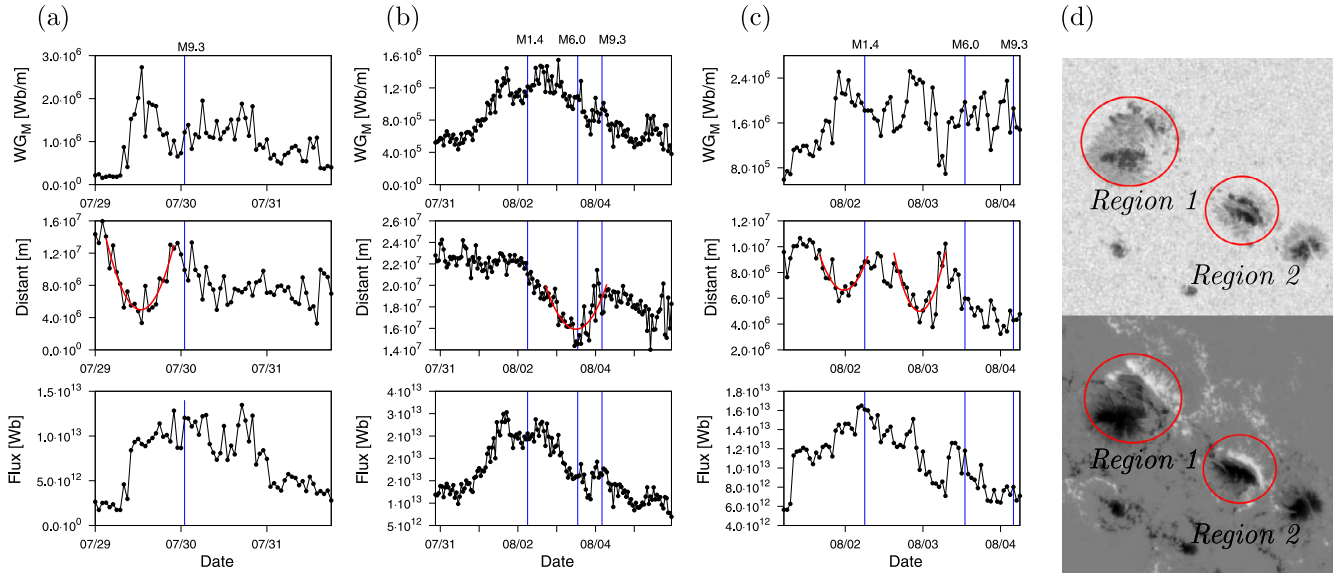

Fig. 1. (a) (b) and (c): Top panel: variation of WG_M as a function of time; Middle panel: evolution of distance between the area-weighted barycenters of the spots of opposite polarities; Bottom panel: unsigned flux of all spots in the encircled area as a function of time. (d): Top panel is intensity and bottom panel is the magnetogram of AR 11261.

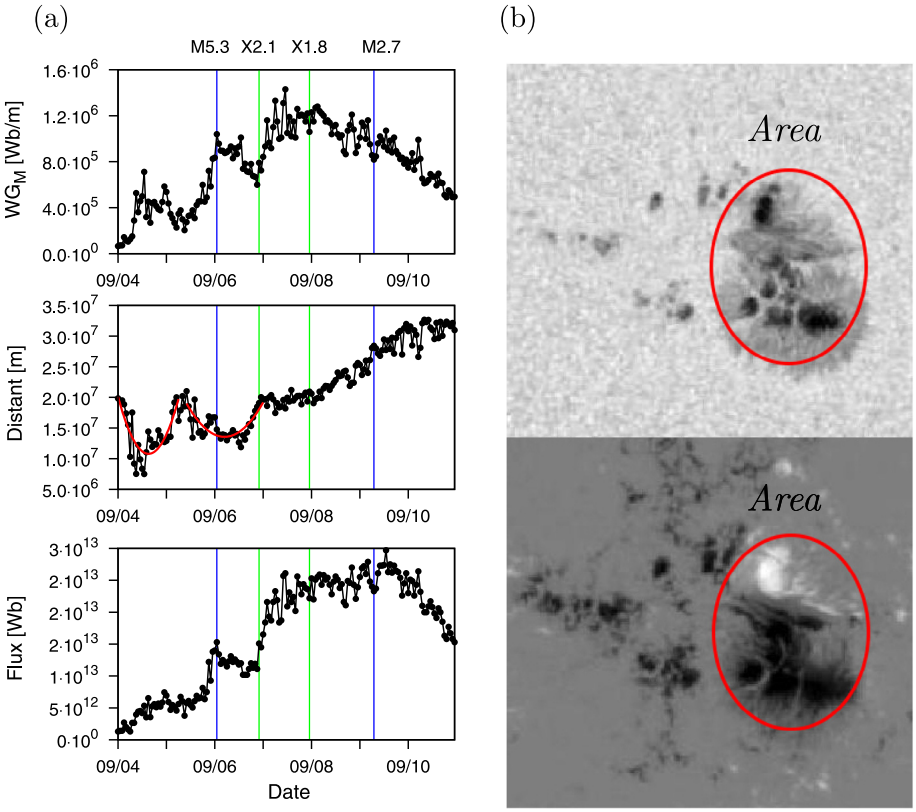

Fig. 2. Same as Fig. 1 but for of AR 11283.

Let us now estimate the predicted maximum flare intensity (S_{flare} in the 1–8 Å wavelength range of GOES) from the maximum value of WG_M according to Eq. (1) of Korsós et al. (2016). The obtained estimated flare classes are in the last but one column of Tables 1–3 for each AR, respectively. The agreement with the measured GOES classification is acceptable but not best. In most cases, only the estimated GOES-class agrees with its measured counterpart. Therefore this tool may require further refinement for a better match. However, this is anyway not the subject

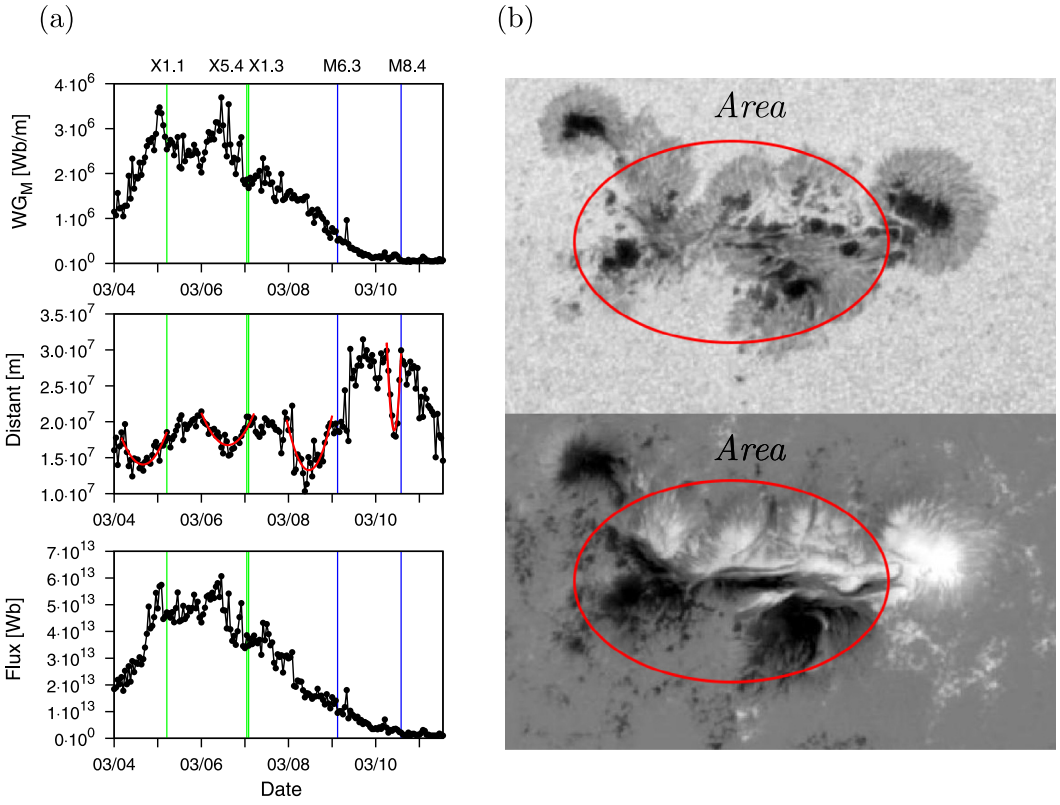

Fig. 3. Same as Fig. 1 but for AR 11429.

of the current work. Next, we also estimate the predicted flare onset times (T_{pred}) from the variation of the time when the distance's converging phase (T_C) start of the distance by the following Equation, in all investigated solar eruptions, namely:

$$T_{pred} = a_1 \cdot T_C + b_1, \quad (2)$$

where $a_1 = 1.29(0.85)$ [h] and $b_1 = 1.11(12.8)$ [h] in the younger (older) than three days case, respectively. In this study, the first M9.3 class-flare of AR 11261 and the M5.3 class-flare of AR 11283 happened before the threshold of 72 h have elapsed, while the further 11 investigated flares all occurred after the 72-h threshold. Therefore for the estimate of the flare onset time of the M9.3 (of AR 11261) and M5.3 (of AR 11283) flares we used $a_1 = 1.29$ [h], and, $b_1 = 1.11$ [h] and for the 11 remaining investigated flares, $a_1 = 0.85$ [h] and $b_1 = 12.8$ [h] were substituted in Eq. (2). In general, one can conclude that Eq. (2) overestimated the flare onset time.

Tables 1–3 summarise the results of the WG_M method, i.e. we listed various properties of the investigated flares and the accompanied linear velocity (v_{lin}) of the CMEs of the three active regions. Furthermore, Tables 1–3 also include the maximum value of WG_M, value of WG_M at the flare onset, duration of the observed compressing phase (T_C), elapsed time between the minimum point until flare onset (T_{D+F}), predicted flare onset time (T_{pred} computed by Eq. (2)), predicted flare intensity (S_{flare} determined by Eq. (1) of Korsós et al., 2016), ratio of maximum value of the WG_M and the value of WG_M at flare onset. The ratio is also an important diagnostic tool of the WG_M method, because as discussed in Korsós et al. (2015), we found that if the value of WG_M decreases over ~54% after the local maxima then no further energetic flare(s) can be expected; but if the maximum of the released flare energy is less than about 42%, further flares are more probable. Furthermore, this diagnostic tool and the onset time estimation (Eq. (2)) should be applied concurrently because occasionally more than one same energetic flare-classes may occur in a short time interval after the U-shaped distance pattern is formed (e.g. Fig. 2).

In brief, we can conclude that the WG_M method has estimated fairly well the expected flare intensity and the onset time. However, the flare-prediction capability of the WG_M method could be further improved by analysing other physical quantities of flaring ARs. Therefore we embarked on investigating the evolution of the total, the shearing and the emerging helicity before flare and CME eruptions for these three cases studies.

2.2. Magnetic helicity method and application to three different AR as test cases

Let us now determine the magnetic helicity associated with the three ARs each, and investigate their evolution prior to the eruptions. The magnetic helicity flux across a surface S introduced by Berger (1984) can be expressed as:

$$\left.\frac{dH}{dt}\right|_S = 2\int_S (\mathbf{A}_p \cdot \mathbf{B}_h)\mathbf{v}_{\perp z} dS - 2\int_S (\mathbf{A}_p \cdot \mathbf{v}_{\perp h})\mathbf{B}_z dS, \quad (3)$$

where $\mathbf{A}_p$ is the vector potential of the potential field $\mathbf{B_p}$. $\mathbf{B}_h$ and $\mathbf{B}_z$ denote the tangential and normal magnetic fields, $\mathbf{v}_\perp$ is the component of the photospheric plasma velocity $\mathbf{v}$ which is perpendicular to the magnetic field, and $\mathbf{v}_{\perp h}$ and $\mathbf{v}_{\perp z}$ are the tangential and normal components of $\mathbf{v}_\perp$. $\mathbf{A}_p$ is determined by the photospheric vertical magnetic field and Coulomb gauge by equations (Berger, 1997; Berger and Ruzmaikin, 2000):

$$\nabla \times \mathbf{A}_p \cdot \hat{\mathbf{n}} = B_h, \nabla \cdot \mathbf{A}_p = 0, \mathbf{A}_p \cdot \hat{\mathbf{n}} = 0. \quad (4)$$

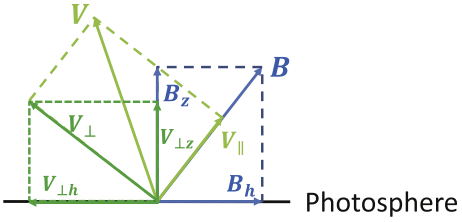

Fig. 4. Diagram of the different components of the photospheric plasma velocity $\mathbf{v}$ and the photospheric magnetic field $\mathbf{B}$.

Based on the basic algebraic relations, we then obtain:

$$v_\parallel = \frac{(\mathbf{v}\cdot\mathbf{B})\mathbf{B}}{B^2}, \quad (5)$$

$$\mathbf{v}_\perp = \mathbf{v} - \frac{(\mathbf{v}\cdot\mathbf{B})\mathbf{B}}{B^2}, \quad (6)$$

$$\mathbf{v}_{\perp h} = \mathbf{v}_h - \frac{(\mathbf{v}\cdot\mathbf{B})\mathbf{B}_h}{B^2}, \quad (7)$$

$$\mathbf{v}_{\perp z} = \mathbf{v}_z - \frac{(\mathbf{v}\cdot\mathbf{B})\mathbf{B}_z}{B^2}. \quad (8)$$

Here, $\mathbf{v}_\parallel$ denotes the velocity components that is parallel to the magnetic field. Fig. 4 demonstrates the different components of v and B in Eqs. (5)–(8).

Solar Dynamics Observatory (SDO) was launched in 2010. The on-board Helioseismic and Magnetic Imager (HMI) is able to map the full disk photospheric vector magnetic field with a high cadence and a long continuity. The vector magnetograms employed in this study are from Space-weather HMI Active Region Patches (SHARPs) with a spatial resolution of 1" and a time cadence of 12 min (Bobra et al., 2014). The photospheric plasma velocity was calculated using the Differential Affine Velocity Estimator for Vector Magnetograms (DAVE4VM) algorithm

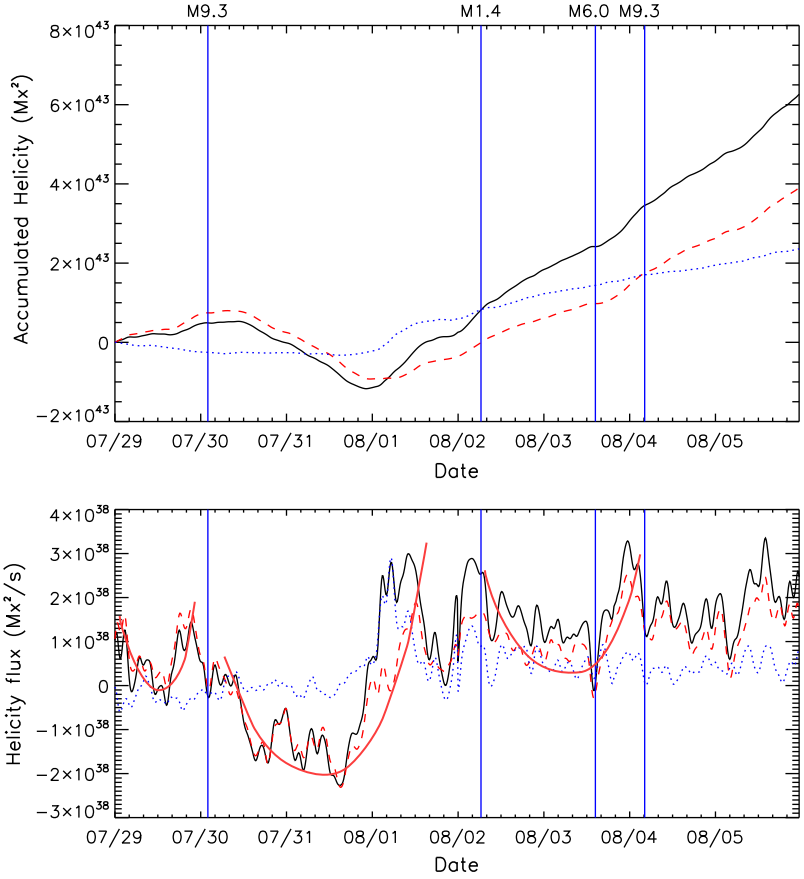

Fig. 5. Top panel: Accumulated helicity from AR 11261; Bottom panel: Helicity flux of AR 11261. The red dashed line and blue dotted line represent the helicity fluxes from shearing motion and from emerging motion, respectively. The black solid line is the total helicity flux. The red parabola highlight the decreasing-increasing phases similar to a feature found in the WG_M results. (For interpretation of the references to colour in this figure legend, the reader is referred to the web version of this article.)

(Schuck, 2008). The window size used in the velocity calculation is 19 pixels, which was determined by examining non-parametric Spearman rank order correlation coefficients, Pearson correlation coefficients and slopes between $\Delta_h \cdot (\mathbf{v}_z\mathbf{B}_h - \mathbf{v}_h\mathbf{B}_z)$ and $\delta\mathbf{B}_z/\delta t$ (Schuck, 2008). The vector potential $\mathbf{A}_p$ is derived using MUDPACK (Adams, 1993), a multigrid software for solving elliptic partial differential equations. Then, we calculated magnetic helicity from these ARs using Eq. (3). The first term on the right side of Eq. (3) is the helicity generated from shearing motions while the second term is the helicity from emerging motions. The helicity flux could be obtained by integrating over the entire calculation area. Magnetic helicity generated by shearing motion and emerging motion were calculated separately, and the total helicity is the combination of the two components.

Temporal profiles of helicity fluxes in the three ARs were plotted in Figs. 5–7. In each figure, the bottom panel is the helicity flux, while the red dashed line is the magnetic helicity flux generated by shearing and twisting movements at the photosphere, the blue dot line stands for that transported across the photosphere, and the black solid line is the total magnetic flux. The top panel shows the accumulated helicity which is obtained by integrating the helicity flux from the start of the observation to the specified time. Also, Fig. 8a-c show the helicity fluxes quantities after normalised by the maximum values of each components separately to show the appropriate scaling.

As there are several data gaps in SHARPs' vector magnetograms from March 3 to March 11, helicity fluxes in Figs. 7 and 8c have been separated into five segments and the accumulated helicity's time sequence was calculated from 00:00:00 UTC, March 4 to 06:36:00 UTC, March 7.

The magnetic helicity flux showed a decrease before every M-class or above flares (see, e.g., Smyrli et al., 2010 and references therein). In AR 11261, the magnetic helicity decreased from the pre-flare highest time to the flare onset time is 1.7×10^{38} Mx^2 s^{-1}, which is 3.6×10^{37} Mx^2 s^{-1}, 1.6×10^{38} Mx^2 s^{-1} and 2.1×10^{38} Mx^2 s^{-1} for the following ARs. In AR 11283, the decrease before each flare is 1.7×10^{38} Mx^2 s^{-1}, 8×10^{37} Mx^2 s^{-1}, 2.1×10^{38} Mx^2 s^{-1} and 1.3×10^{38} Mx^2 s^{-1}. The total helicity flux in AR 11429 is negative, the absolute value had a decrease of 1.2×10^{39} Mx^2 s^{-1} in the first X1.1 flare, and a total of 1.8×10^{39} Mx^2 s^{-1} change in the following two X-class flares. Three X- and two M-class flares have been produced in AR 11429 with a corresponding much higher helicity injection than that in the other two ARs (AR 11261 and AR 11283). It suggests that large helicity flux which injects magnetic free energy continuously into the solar atmosphere may results in fierce

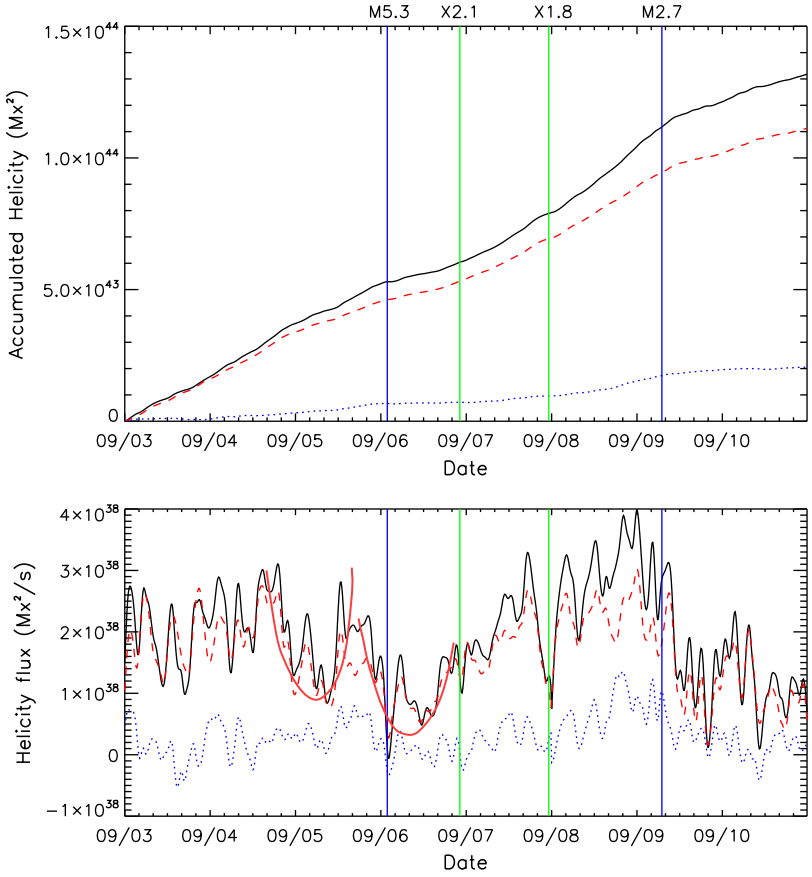

Fig. 6. Same as Fig. 5 but for AR 11283.

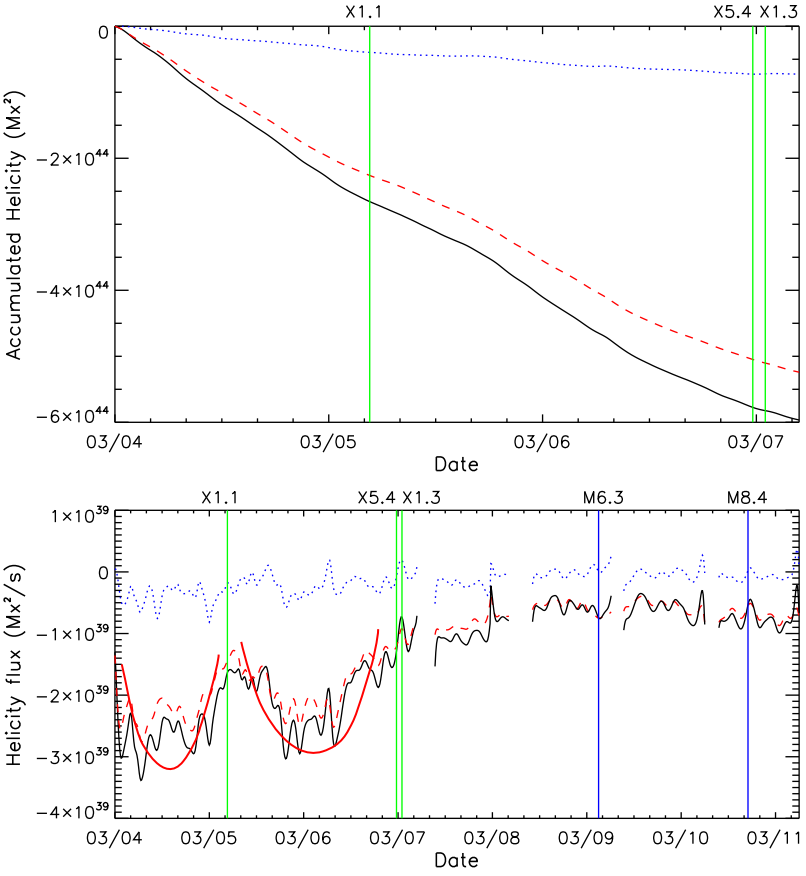

Fig. 7. Same as Fig. 5 but for AR 11429.

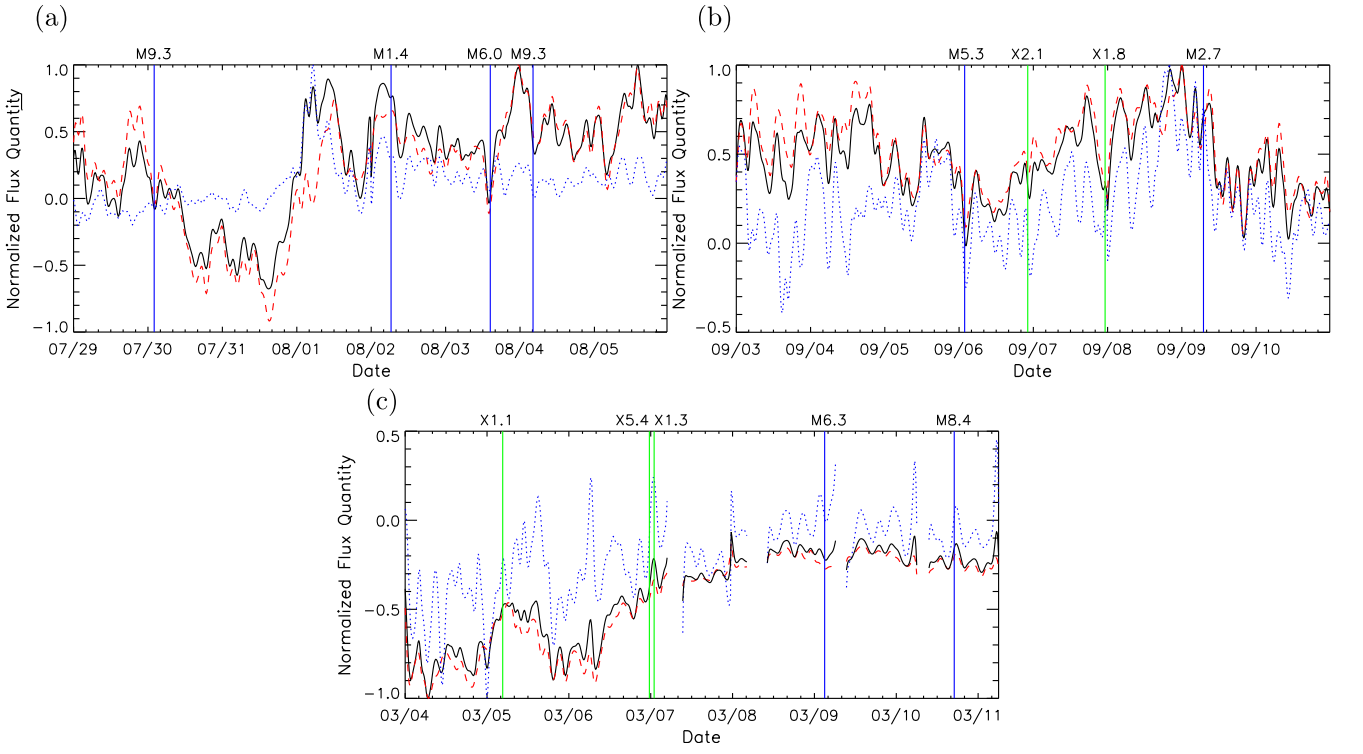

Fig. 8. Helicity flux of AR 11261 (a), AR 11283 (b) and AR 11429 (c) normalised by the maximum values of the helicity flux changes, the representations of different helicity flux components is the same with Figs. 5–7.

flare eruptions. Also, the magnetic helicity flux from emerging motion was more stable than that from shearing motion which fluctuated considerably during the AR's life time. It also can be found that before large flares, the helicity flux from shearing motion dominated the helicity accumulation, which indicates its essential position in solar eruptions.

Besides, several clear long-duration decreasing-increasing phases could be found in either the total helicity flux or the shearing helicity flux before large flares. Some of them even covered a day during the entire phase. Strong shearing movement along the PIL introduced large shearing helicity fluxes with opposite sign on both sides of it, resulting in a downward trend in the total shearing helicity flux in the entire area of interest. When such shearing motion became weak, the total shearing helicity would then increase with the domination of one polarity's helicity flux.

3. Conclusion

There are several flare-forecasting methods based on photospheric observations of the ARs in the solar atmosphere. Here, we applied two different approaches to develop the basics of a good and reliable flare and CME prediction tracking model (for reviews see Benz, 2017; Leka et al., 2017 and references therein). One approach is the weighted horizontal magnetic gradient method (denoted as WG_M) introduced in Korsós et al. (2015) and the second one is the magnetic helicity method (Berger, 1984; Berger and Field, 1984). We applied these two methods to three different flare- and CME-rich ARs, namely AR 11261, AR 11283 and AR 11429. All three active regions produced a series of solar eruptive occurrences. AR 11261 hosted four M-class flares and a fast CME after one M-class falre. AR 11283 had similar activity like AR 11261 with two M- and two X-class flares, and a slow CME. AR 11429 was the most powerful of the three active regions with five compact and large solar eruptions.

Applying the first investigation, we followed the temporal evolution of WG_M and the distance between the area-weighted barycenters of opposite polarities within an appropriately defined region close to PIL of the three studied ARs. During the empirical analyses of the three ARs, first, we recognised typical pre-flare behaviour patterns of WG_M and distance likewise in Korsós et al. (2015). One remarkable behaviour of the evolution of the opposite polarities is that there is indeed the steep rise and the maximum value of the magnetic flux gradient followed by a less steep decrease before the flare and CME occurrences. Parallel to the increasing/decreasing trends of WG_M, concurrent decreasing/increasing (approaching/receding) trends of distances, called as the U-shaped pattern, were also observed during the evolution of the opposite polarity spots.

The second approach was the employing magnetic helicity calculation. We separately followed the evolution of the total, emerging and shearing helicity components prior the flare and CME occurrences. To clearly track the evolution of magnetic helicity flux, the total magnetic helicity was divided into two terms. One is from the emergence of twisted field lines that cross the photospheric surface, which is the so-called emerging helicity. The other one is from the shearing motion in the photosphere that twisting field lines, which is where the shearing helicity comes from (Berger, 1984; Berger and Field, 1984).

In the evolution of helicity flux, we recognized similar decreasing-increasing phases in the shearing and total helicity flux terms before the flare(s) and CME(s) occurred, just as that been found as the decreasing-receding phase of flares when applying WG_M. This common property is highlighted by red parabola in Figs. 1–3 and 5–7. We can also conclude that the duration of the decreasing-increasing phases is very comparable during the evolution of shearing helicity flux and the distance between the area-weighted barycenters of the spots of opposite polarities. Furthermore, we note that we cannot determine any meaningful behaviour in the evolution of the emerging helicity. Therefore, it is worth pointing out that the shearing motion may play a more important role in the formation of total helicity because the value of emerging helicity is negligible when compared to the value of the shearing helicity.

According to our empirical case studies, we can clearly identify a *common decreasing-increasing phase* in the evolution of *shearing helicity* and *weighted distance* prior to flare and CME eruptions (see Figs. 1–3 and 5–7). This new result is really interesting, because we may conclude that the shearing mechanism may also be an equally key driver for the solar eruption, and perhaps not only the so much studied emerging process is relevant. In the literature, there are several flare and CME models based on the photospheric shearing motion. Sturrock and Coppi (1966) introduced the tearing-mode instability model which is based on the shearing motion at the photosphere, or there is the model of sheared loops inside arcade by Somov et al. (1998). The magnetic breakout model, presented by Antiochos et al. (1999) is also based on photospheric shearing motions. But the emerging flux process seems to be more favoured and more widely acceptable (see, e.g., Chandra et al., 2009; Takafumi and Takaaki, 2014; Louis et al., 2015 and references therein) when trying to understand flare/CME eruption dynamics. We propose, this latter view may need to be revised in light of our case studies.

We would also emphasise that we do not say that the emerging process is not needed for analysing or predicting large-scale solar eruptions. On the contrary, without flux emergence, there is likely to be no flaring. Finally, we argue that there is a need for a much larger statistical study in order to confirm our conjecture formulated in this work. However, this is beyond the scope of the present case studies.

Acknowledgements

We acknowledge the use of HMI SHARPs data from SDO/HMI team. This work is supported by the National

Science Foundation of China (NSFC) under Grant No. 41231068. YDY is grateful for the support from the State Key Laboratory of Space Weather, National Space Science Center, CAS. MBK is grateful to the University of Sheffield for the support received while carrying out part of the research there. RE is grateful to Science and Technology Facilities Council (STFC) UK and the Royal Society (UK). The authors also acknowledge the support received from the CAS Key Laboratory of Solar Activity, National Astronomical Observatories Commission for Collaborating Research Program. RE acknowledges the support received from the CAS Presidents International Fellowship Initiative, Grant No. 2016VMA045.

References

Adams, J., 1993. MUDPACK-2: multigrid software for elliptic partial differential equations on uniform grids with any resolution. Appl. Math. Comput. 53, 235–249.

Antiochos, S.K., DeVore, C.R., Klimchuk, J.A., 1999. A model for solar coronal mass ejections. Astrophys. J. 510, 485–493.

Baranyi, T., Györi, L., Ludmány, A., 2016. On-line tools for solar data compiled at the debrecen observatory and their extensions with the greenwich sunspot data. Solar Phys. 291, 3081–3102.

Benz, A.O., 2017. Flare observation. Liv. Rev. Solar Phys. 14 (2), 59.

Berger, M.A., 1984. Rigorous new limits on magnetic helicity dissipation in the solar corona. Geophys. Astrophys. Fluid Dyn. 30, 79–104.

Berger, M.A., Field, G.B., 1984. The topological properties of magnetic helicity. JFM 147, 133–148.

Berger, M.A., 1997. Magnetic helicity in a periodic domain. J. Geophys. Res. 102, 2637–2644.

Berger, M.A., Ruzmaikin, A., 2000. Rate of helicity production by solar rotation. J. Geophys. Res. 105, 10481–10490.

Bobra, M.G., Sun, X., Hoeksema, J.T., Turmon, M., Liu, Y., Hayashi, K., Barnes, G., Leka, K.D., 2014. The Helioseismic and Magnetic Imager (HMI) vector magnetic field pipeline: SHARPs - space-weather HMI active region patches. Solar Phys. 289, 3549–3578.

Chandra, R., Schmieder, B., Aulanier, G., Malherbe, J.M., 2009. Evidence of magnetic helicity in emerging flux and associated flare. Solar Phys. 258, 53–67.

Démoulin, P., 2007. Recent theoretical and observational developments in magnetic helicity studies. Adv. Space Res. 39, 1674–1693.

Démoulin, P., Pariat, E., 2009. Modelling and observations of photospheric magnetic helicity. Adv. Space Res. 43, 1013–1031.

Hagyard, M.J., Venkatakrishnan, P., Smith Jr., J.B., 1990. Nonpotential magnetic fields at sites of gamma-ray flares. Astrophys. J. Suppl. Ser. 73, 159–163.

Hudson, H., 2010. Observations of solar and stellar eruptions, flares, and jets. In: Schrijver, Carolus J., Siscoe, George L. (Eds.), Heliophysics: Space Storms and Radiation: Causes and Effects. Cambridge University Press, London, p. 123, ISBN: 9780521760515.

Korsós, M.B., Ludmány, A., Erdélyi, R., Baranyi, T., 2015. On flare predictability based on sunspot group evolution. Astrophys. J. 802, L21–L27.

Korsós, M.B., Ruderman, M.S., 2016. On flare and CME predictability based on sunspot group evolution. In: Dorotovic, Ivan, Fischer, Catherine E., Temmer, Manuela (Eds.), Coimbra Solar Physics Meeting: Ground-based Solar Observations in the Space Instrumentation Era Proceedings of a Meeting held at the University of Coimbra, Coimbra, Portugal In 5–9 October 2015, ASP Conference Series, vol. 504. Astronomical Society of the Pacific, San Francisco, pp. 43–48.

Leka, K.D., Barnes, G., Wagner, E.L., 2017. Evaluating (and improving) estimates of the solar radial magnetic field component from line-of-sight magnetograms. Solar Phys. 292, 36–62.

Louis, Rohan E., Kliem, Bernhard, Ravindra, B., Chintzoglou, Georgios, 2015. Triggering an eruptive flare by emerging flux in a solar active-region complex. Solar Phys. 290, 3641–3662.

Nindos, A., Andrews, M.D., 2014. The association of big flares and coronal mass ejections: what is the role of magnetic helicity? Astrophys. J. 616, L175–L178.

Roudier, T., Svanda, M., Meunier, N., Keil, S., Rieutord, M., Malherbe, J.M., Rondi, S., Molodij, G., Bommier, V., Schmieder, B., 2008. Large-scale horizontal flows in the solar photosphere. III. Effects on filament destabilization. Astron. Astrophys. 480, 255–263.

Schrijver, C., 2007. A characteristic magnetic field pattern associated with all major solar flares and its use in flare forecasting. Astrophys. J. 655, L117–L120.

Schuck, P.W., 2008. Tracking vector magnetograms with the magnetic induction equation. Astrophys. J. 683, 1134–1152.

Smyrli, A., Zuccarello, F., Romano, P., Zuccarello, F.P., Guglielmino, S. L., Spadaro, D., Hood, A.W., Mackay, D., 2010. Trend of photospheric magnetic helicity flux in active regions generating halo coronal mass ejections. Astron. Astrophys. 521 (A56), 12.

Somov, Boris V., Kosugi, Takeo, Sakao, Taro, 1998. Collisionless three-dimensional reconnection in impulsive solar flares. Astrophys. J. 497, 943–956.

Sturrock, P.A., Coppi, B., 1966. A new model of solar flares. Astrophys. J. 143, 3–23.

Takafumi, K., Takaaki, Y., 2014. Simulation study of solar plasma eruptions caused by interactions between emerging flux and coronal arcade fields. Astrophys. J. 796, 44–57.

Yashiro, S., Akiyama, S., Gopalswamy, N., Howard, R.A., 2006. Different power-law indices in the frequency distributions of flares with and without coronal mass ejections. Astrophys. J. 650, L143–L146.

Zhang, Y., Kitai, R., Takizawa, K., 2012. Magnetic helicity transported by flux emergence and shuffling motions in solar active region Noaa 10930. Astrophys. J. 751, 85–91.